

Synthetic Light-in-Flight

PATRICK CORNWALL^{1,*}, MANUEL BALLESTER², STEFAN FORSCHNER¹,
MURALIDHAR MADABHUSHI BALAJI¹, AGGELOS KATSAGGELOS^{2,3}, AND FLORIAN WILLOMITZER^{1,2,3,*}

¹Wyant College of Optical Sciences, University of Arizona, Tucson, AZ, 85721, USA.

²Department of Computer Science, Northwestern University, Evanston, IL 60208, USA.

³Department of Electrical and Computer Engineering, Northwestern University, Evanston, IL 60208, USA.

*patrickcornwall@arizona.edu, fwillomitzer@arizona.edu

Light-in-flight (LiF) measurements allow to resolve and visualize the path that light travels through an arbitrary volumetric scene. Traditional LiF methods involve expensive high-speed electronics or narrow-pulse light sources. We present a novel computational LiF approach that only requires continuous-wave (CW) lasers and off-the-shelf CMOS cameras to capture the full LiF information about the scene. From multiple CW scene measurements at different optical wavelengths, we create multiple “synthetic fields,” each at a “synthetic wave” which is the beat wave of two respective optical waves. Due to their robustness to speckle, the synthetic fields can be computationally combined into a “synthetic light pulse,” which precisely sections the volumetric scene. Moreover, the complex synthetic fields can be freely manipulated in the computer after their acquisition, which allows for spatial and temporal shaping of different sets of pulses from the same set of measurements to maximize the decoded information output for each scene. In addition, the relative speed at which the pulse travels through the scene can be used to characterize physical scene properties such as depth or indices of refraction.

1. INTRODUCTION

Although many years have passed since light-in-flight (LiF) measurements were first demonstrated [1–5], visualizations of a light pulse traveling through a volumetric scene and interacting with embedded objects, has still not lost its “magical effect” on the observer. Today, light-in-flight (LiF) imaging (i.e., the ability to resolve light itself in space and time at high frame rates as it propagates through a volumetric scene) has developed into a powerful method to observe light-related ultrafast phenomena, which in turn enables numerous potential imaging applications in biomedical imaging, industrial inspection, or virtual reality. Examples include observing light propagation through heterogeneous material or tissue [3, 6–8], characterization of manufac-

tured components [9, 10], and the development of innovative viewpoint rendering techniques [11].

State-of-the-art LiF techniques generally capture LiF videos by launching ultra-short light pulses into a medium or volumetric scene and recording the response with a high-speed detector such as a single-photon avalanche diode (SPAD) or a streak camera [5, 12–16]. As an example, the iconic “soda bottle video” [12] was captured using this kind of approach, and related LiF concepts triggered important follow-up ideas in research fields such as non-line-of-sight (NLoS) imaging or imaging through scattering media [7, 17–22].

In this paper, we present a novel computational approach to LiF imaging that completely eliminates the need for high-speed equipment. Instead, our technique uses ordinary CMOS detectors and (tunable) continuous-wave (CW) laser sources. Our approach draws inspiration from interferometric and holographic LiF approaches that have been proposed over the years [3, 4, 23–25], but specifically builds upon the concept of “synthetic wavelength imaging” (SWI), which has been utilized for various applications in 3D imaging of rough surfaces, NLoS imaging, and imaging through scattering media and optical fibers [26–39]: When coherent light is reflected off a rough surface or transmitted through a scattering medium, the phase randomization in the arising speckle field hinders the extraction of distance or time-of-flight information from an interferometric measurement. SWI addresses this problem by exploiting spectral correlations in speckle fields captured at slightly different wavelengths λ_1 and λ_2 . Combining these two speckle fields $E(\lambda_1)$, $E(\lambda_2)$ creates a high frequency carrier wave with a low frequency beat note. The wavelength of this beat wave can be described by the “synthetic wavelength” [28, 30] $\Lambda = \lambda_1 \cdot \lambda_2 / |\lambda_1 - \lambda_2|$. For closely spaced λ_1 and λ_2 , which results in a large Λ , the computationally generated “synthetic field” $E(\Lambda)$ is largely robust to the phase perturbations in an optical speckle field, and hence can be used for interferometric phase measurements of light transmitted through a scattering medium or reflected off a rough surface. Related evaluations happen purely computationally at the much larger synthetic wavelength Λ .

In the following sections of this paper, we describe our “Synthetic LiF” (SLiF) approach and provide proof-of-principle experimental results, serving as a first-ever demonstration of pulsed SLiF measurements in a variety of volumetric 3D scenes, scenes with varying refractive indices, and scattering media with embedded foreign bodies. Additionally, we demonstrate for the

first time how SLiF pulses can be computationally shaped and manipulated in time and space *after* their acquisition to highlight various features and maximize the decoded information output for each measured scene.

2. FROM SYNTHETIC WAVES TO SYNTHETIC PULSES

As described in [28, 30], one method for generating the unspeckled synthetic field $E(\Lambda)$ is by computationally mixing the two captured speckle fields $E(\lambda_1)$ and $E(\lambda_2)$ (see Fig. 1):

$$\begin{aligned} E(\Lambda) &= E(\lambda_1) \cdot E^*(\lambda_2) \\ &= A_{\lambda_1} A_{\lambda_2} \cdot e^{i(\phi(\lambda_1) - \phi(\lambda_2))} = A_{\Lambda} \cdot e^{i\phi(\Lambda)} \end{aligned} \quad (1)$$

In the case that $E(\lambda_1)$ and $E(\lambda_2)$ are emitted and captured sequentially, their beat wave (synthetic wave) has never physically existed and only exists in the computer. Nevertheless, the complex synthetic field $E(\Lambda)$ largely possesses the characteristics of a conventional electromagnetic field at wavelength Λ . In particular, if λ_1 and λ_2 are closely spaced, the synthetic field's phase term $\phi(\Lambda) = \phi(\lambda_1) - \phi(\lambda_2)$ is robust to microscopic path length variations introduced when light is reflected off an optically rough surface or propagates through a scattering medium [28, 30].

One key contribution of this paper lies in the realization of how the concept of synthetic waves can be used for pulsed LiF measurements. The proposed procedure exploits another striking analogy between synthetic waves and optical waves: For pulse generation in the optical domain (e.g., in a pulsed laser), light fields at multiple wavelengths are synced in phase and simultaneously emitted so that their superposition in space forms a light pulse. To generate and capture a “synthetic pulse”, we perform the “computational synthetic wave equivalent” of optical pulse generation: The basic idea is to capture multiple synthetic fields $E(\Lambda_n)$ ($n = 1, \dots, N$), each generated from a pair of captured optical fields $E(\lambda_j)$ and $E(\lambda_l)$, and eventually superimpose all $E(\Lambda_n)$ computationally after their acquisition to form the synthetic pulse P [38].

We emphasize, however, that drift prevents the phases of the captured fields $E(\Lambda_n)$ from being aligned after their acquisition and that an alignment procedure has to be performed prior to their superposition. Notably, the unique properties of synthetic fields (in particular, their smooth, unspeckled phase front) allow us to perform this alignment completely computationally after the acquisition: As shown in Eq. 1, each generated synthetic field is assigned a synthetic amplitude A_{Λ} and synthetic phase $\phi(\Lambda)$, both of which may be freely manipulated in the computer after acquisition. For example, we can add a global phase offset to all phase values in the 2D arrays of every captured synthetic field $E(\Lambda_n)$. To now computationally align the phase values in all captured fields, we observe the phases $\phi(\Lambda_n, x_o, y_o)$ at an arbitrary scene point (x_o, y_o) . Eventually, we add a global phase offset $\Delta\phi_n$ to each individual synthetic field (new phase: $\tilde{\phi}(\Lambda_n) = \phi(\Lambda_n) + \Delta\phi_n$), satisfying the condition that all phase maps for all fields arrive at the same phase value in point (x_o, y_o) :

$$\tilde{\phi}(\Lambda_1, x_o, y_o) = \tilde{\phi}(\Lambda_2, x_o, y_o) = \dots = \tilde{\phi}(\Lambda_N, x_o, y_o) \quad (2)$$

Additionally, we replace the (speckled) amplitude A_{Λ_n} of each synthetic field with an array of ones ($\tilde{A}_{\Lambda_n} = 1$) to mitigate speckle artifacts in our final pulse reconstruction. With each computationally manipulated synthetic field $\tilde{E}(\Lambda_n) = \tilde{A}_{\Lambda_n} \cdot e^{i\tilde{\phi}(\Lambda_n)}$

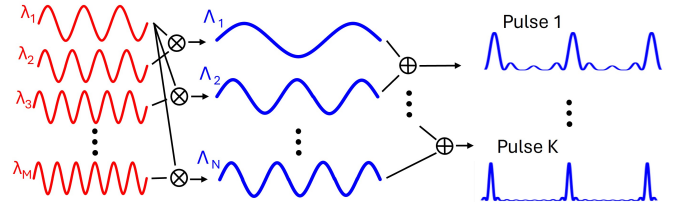


Fig. 1. Generation of synthetic pulses: A set of captured optical fields at different wavelengths $\lambda_1, \dots, \lambda_M$ is used to create a set of synthetic fields at synthetic wavelengths $\Lambda_1, \dots, \Lambda_N$, e.g., via computational pairwise mixing. Eventually, the synthetic fields are computationally superimposed to create a synthetic pulse train. The pulse becomes more well-defined the more synthetic fields are added.

the synthetic pulse is then assembled via

$$P(\Lambda_1, \dots, \Lambda_N) = \tilde{E}(\Lambda_1) + \tilde{E}(\Lambda_2) \dots + \tilde{E}(\Lambda_N) . \quad (3)$$

Due to the computational phase alignment at scene point (x_o, y_o) , calculation of the intensity term $|P|^2$ produces a “synthetic pulse maximum” at (x_o, y_o) , and all scene points that observe the same optical path length distance (see, e.g., Fig. 2a-d). This results in a pulse front which is then computationally advanced over the scene by simply advancing the time variable in the synthetic phase term. The outcome is a SLiF video that reveals how the synthetic pulse has traveled through the volumetric scene (see next sections and Figs. 2 and 3). We note that this computational advancement in time can be performed in arbitrarily fine time increments, meaning that the temporal frame resolution of each SLiF video can be infinitely high and is not limited by any hardware constraints. In turn, this means that the often used *concept of camera frame rate as a measure of temporal resolution does not apply to SLiF*. The temporal resolution (which is directly proportional to the depth resolution or the measured scenes) is solely defined by the width of the synthetic pulse, which can be readily deduced based on the given Fourier relationships. One possibility to quantify the pulse width is by evaluating the full-width-at-half-maximum (FWHM) of the synthetic pulse, which is mainly proportional to the inverse of the total captured optical wavelength range $|\lambda_1 - \lambda_M|$ and the number of captured (synthetic) fields. Another important factor is the pulse period, which determines the unambiguous measurement range, and is mainly dependent on the inverse of the smallest spacing between captured individual optical wavelengths, $|\lambda_j - \lambda_{j-1}|$. Both quantities can be equivalently expressed using synthetic wavelength spacings and are ultimately constrained by the wavelength sampling as defined, e.g., by the tuning characteristics of the used laser.

With the exception of Fig. 3d (see caption), all measurements presented in this paper have been captured at 41 roughly equidistantly spaced optical wavelengths within a range of 854.20nm to 856.05nm (ultimately limited by the maximal tuning range of our lasers), which corresponds to 40 distinct synthetic wavelengths. The actual used wavelength range for each measurement varies depending on the depth of the actual scene being captured. Shallow scenes, which require less unambiguous distance, are captured with larger separations between wavelengths compared to scenes with greater depth. Our measurement with the largest optical wavelength range $\Delta\lambda = 1.85nm$ shown in 3a demonstrates an experimentally evaluated pulse FWHM of 0.57ps which corresponds to a depth resolution of 170μm. Higher resolutions can be achieved by larger wavelength ranges.

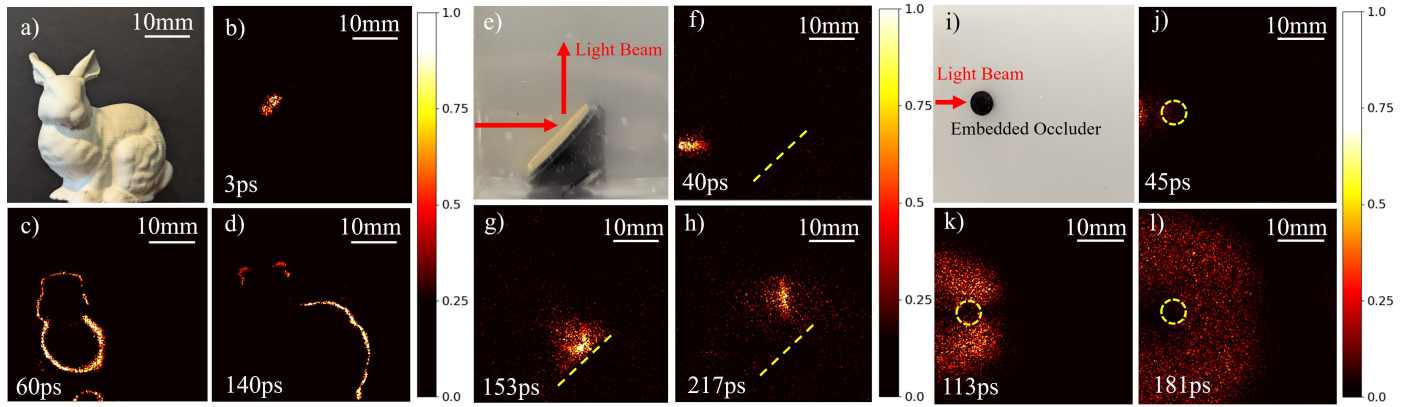


Fig. 2. Synthetic pulse propagation through volumetric 3D scenes and scattering media (see videos [here](#) [40]): a-d) Synthetic pulse propagation at different time stamps (b-d) across a 3D-printed bunny object (a). Experimentally evaluated pulse FWHM for this measurement: $9.88ps$ or $2.96mm$. e-h) Reflection of synthetic pulse at mirror embedded in lightly scattering medium (e), shown at different stamps (b-d). i-l) Synthetic pulse traversing through a strongly scattering medium with embedded "foreign object" (i). Photon horizon at different time stamps (j-l).

To capture the required optical fields fast and with high pixel resolution, we use the single-shot procedure introduced in [31]. Although the described setup would allow us to capture each synthetic field $E(\Lambda_n)$ (i.e., two optical fields) in single-shot, we herein limit ourselves to the single-shot capture of each individual optical field $E(\lambda_n)$ due to the slightly better noise characteristics described in [31].

A. Synthetic Pulse propagation through a volumetric scene

The first measurement, shown in Fig. 2a-d, depicts the propagation of a synthetic pulse front across a 3d printed bunny figure (Fig. 2a). The scene is flood illuminated at the different wavelengths by a distant fiber tip, meaning that the pulse front that hits the printed bunny is not perfectly planar (i.e., parallel to the x-y-plane), but rather slightly spherical. Figure 2b-d shows the advancement of the pulse front over the bunny surface at selected time stamps ($3ps$, $60ps$, $140ps$). The synthetic pulse front can be seen traveling through the scene and sectioning the bunny surface at different depth values. We encourage the reader to view the rendered SLiF videos [here](#) [40]. Besides visualizing the SLiF video, the presented information could be used, e.g., to calculate a precise 3D model of the object. For the optical tuning range in this measurement of $854.2nm$ to $854.43nm$, the experimentally evaluated FWHM of the visualized synthetic pulse $|P|^2$ is $9.88ps$ which corresponds to $2.96mm$.

The experiment shown in Fig. 2e-h depicts the propagation of a synthetic pulse packet through a scattering medium and its interaction with a reflecting mirror. Here, a tightly collimated laser beam is launched perpendicular to the optical axis towards a 45° angled mirror, which is embedded in a weakly scattering medium to make the light beam visible. It can be seen that the synthetic pulse propagates through the medium, hits the mirror, and continues in a different direction as dictated by the law of reflection (see video [here](#) [40]).

B. Synthetic Pulse propagation through a scattering medium

The experiment shown in Fig. 2i-l showcases how the SLiF framework can be used to visualize the "photon horizon", seen when a light pulse interacts with a strongly scattering medium containing an embedded occluder ("foreign object"). Again, a tightly collimated beam is launched perpendicular to the optical axis into the scattering medium and the scattered light is viewed

from an orthogonal orientation relative to the propagation direction. While the synthetic pulse is advancing and spread through the scatterer, one can observe the propagating photon horizon, as it is blocked by the occluder and eventually scatters back into its geometrical shadow.

3. SYNTHETIC PULSE SHAPING

One of the distinct advantages of our computational SLiF approach is the ability to manipulate pulse measurements *after* they have been acquired. Besides the basic phase alignment of all synthetic fields which was discussed in the last section, this unique property can be further expanded to *freely shape the synthetic pulse in time and space*. From an information-theoretical perspective, this temporal and spatial pulse shaping is equivalent of changing the information *decoder* [41–43], and can be used to highlight or visualize different aspects or properties of the measured scene.

A. Temporal Pulse Shaping

The experiments described in the last section involve the superposition of synthetic fields, where each field is added with aligned phases and constant amplitudes. Due to the Fourier pair relationship between added fields and pulse shape, the resulting pulse train P takes the form of a repeating *sinc* function in the temporal domain. This can be observed in Fig. 3a: The experiment shows a synthetic pulse front incident on a planar ground glass diffuser. The light is emitted from a point source (fiber tip) centered behind the diffuser, which results in a pulse front in the spatial shape of an expanding circle (see also video [here](#) [40]). For the used optical wavelength range between $854.2nm$ and $856.05nm$, the experimentally evaluated FWHM of the synthetic pulse $|P|^2$ is $0.57ps$ or $170\mu m$.

Given the fact that each synthetic field used to create the pulse train can be computationally manipulated individually, it is now possible to adjust the amplitude \hat{A}_{Λ_n} of each field to produce different temporal pulse shapes *from the same set of measurements after their acquisition*. For example, adjusting the \hat{A}_{Λ_n} values to fit a Hann windowing function rather than a rectangle in the Fourier domain results in an apodized pulse shape (Fig. 3b, FWHM of $|P|^2$ is $2.07ps$ or $621\mu m$). If a *sinc* distribution is selected in the Fourier domain, a rectangular pulse shape will

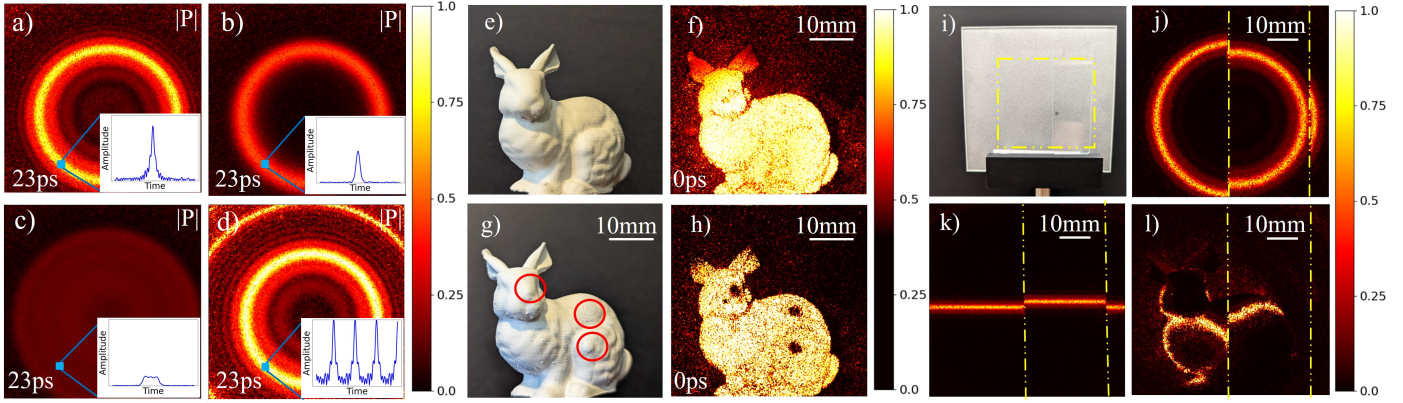


Fig. 3. Synthetic pulse shaping and evaluation of material properties (see videos [here](#))[40]: a-d) Temporal pulse shaping of a spherical synthetic pulse front incident on a planar diffuser. Windowing functions: a) Rectangular, b) Hann window, c) *sinc*-function, d) Rectangular function, but only 11 synthetic fields over an optical wavelength range between $854.2nm$ and $856.05nm$ are used. Note that (a-d) plot $|P|$ instead of $|P|^2$ for better visibility of the temporal profiles e-h) Spatial pulse shaping by computationally delaying the synthetic pulse front with a different value in each scene point. A "bunny-shaped" pulse front hits all surface points of a 3D printed bunny object (e) at the same time (f). Using the same bunny-shaped wavefront to illuminate a similar bunny object with small $\sim 1mm$ thick applied defects (g), enables immediate visual identification of the defects (h). i-l) Synthetic pulse front, delayed by optical path length difference of a $1mm$ thick glass slide. Planar diffuser, half covered with glass slide (i), illuminated by spherical synthetic pulse from behind (j). Synthetic pulse shaping allows for additional forms to decode increased optical path length. Pulse front offset clearly visible in a horizontal "scan line" (k) from a planar vertically tilted pulse front, and also in a bunny-shaped pulse front (l) illuminating diffuser and glass slide.

appear in the temporal domain (Fig. 3c). Moreover, it is possible to select a subset of the measured fields to adjust the length of the pulse train. By selecting fields with larger wavelength difference, the pulse train period is shortened so that a full period becomes observable in the given field of view (Fig. 3d). We note that Figs. 3a-d depict $|P|$ instead of $|P|^2$ for better visibility of the temporal profiles. The figures also show a plot of each temporal pulse profile, by selecting a single point in the rendered scene and graphing the amplitude in this point as a function of time (see video [here](#)[40]).

Besides the numerous advantages of computationally sharpening or broadening the pulse peak after the measurements have been acquired, we envision several other potential, future applications of temporal pulse shaping. For example, pulse pairs with a precisely defined distance could serve as a "temporal ruler" that could be flexibly moved back and forth in the computer to measure time or depth differences in the scene. In full-field mode, this could potentially be used as an "adjustable virtual strobe illumination" whose frequency could be selected very high, and dynamically changed after acquisition. Our pulse shaping approach could also be developed in a computational variant of earlier holographic pulse shaping approaches demonstrated, e.g., in [44, 45]. In another application scenario, a synthetic pulse sequence with different temporal shapes and intensity levels could be produced, which could potentially be used as a "temporal code," similar to what has been proposed in [46] for amplitude-modulated time-of-flight cameras that work at much lower temporal and depth resolution.

B. Spatial Pulse Shaping

In addition to the temporal pulse response shaping described above, a second type of computational pulse shaping is possible after measurement collection: spatial shaping. Spatial pulse shaping can be used to change the 3D spatial shape of the syn-

thetic pulse front. An illustrative example would be to turn a spherical pulse front (as emitted from our point source-like fiber tip) into a planar pulse front. We perform this spatial shaping by computationally delaying the synthetic pulse front, where each scene point (pixel) receives a different delay so that a certain pulse front can be shaped. After calibrating the initial 3D pulse shape produced by the setup (e.g., by taking a "calibration measurement" of a planar surface, similar to Fig. 3a or b), we computationally add a custom phase delay to every pixel (x, y) of each synthetic field $E(\Lambda_n)$. This phase delay is calculated from the difference between the calibrated 3D pulse shape and the "target 3D shape" of the desired pulse front. We emphasize that this "target 3D shape" could be a mathematical function (plane, sphere, paraboloid, etc.) or a freeform 3D shape (bunny, face, technical part, etc.). The 3D shape can be imported from a CAD-file, measured by an independent 3D sensor, or even measured with the sensor introduced in this paper¹. Figures 3e-h visualize the process of spatial pulse shaping and a potential application: After taking a SLiF measurement of a scene with a printed 3D object (bunny) and performing the steps mentioned above, the object is virtually illuminated with a synthetic pulse front that has been spatially reshaped to the 3D shape of a bunny. As all points in the bunny-shaped pulse front hit the surface of the 3D object at the same time, all surface points "flash up" simultaneously for one time stamp (arbitrarily set to $0ps$ in Fig. 3f and h). In a following step, we add small surface "defects" by applying small white paint droplets to the surface of the printed object. An image of the bunny figure "with defects" is shown in Fig. 3g. Each defect is only approximately $3mm$ wide and $1mm$ thick, and spotting the defects in the conventional camera image of Fig. 3g is nearly impossible. However, when illuminating the 3D object (with defects) with the previously

¹Although not the focus of this paper, we emphasize that a "byproduct" of our SLiF measurements is a very precise 3D model of the measured scene.

created bunny-shaped wavefront (without defects), the three applied defects are immediately visible in the image produced for the $0ps$ timestamp (Fig. 3g), as the pulse front now differs from the true 3D shape at the positions of the defects. We believe that this measurement highlights the great potential of our method for defect detection in industrial inspection, but also to detect irregularities in medical images, forensic scenes, or works of art. An image like Fig. 3g can easily be processed with basic image processing algorithms and fed into existing pipelines, e.g., in a production line.

C. Material Properties

Although the pulses presented in this paper do not physically exist and only exist in the computer, they are still subject to the physics of the scene. An example of this can be shown by observing the material properties of the objects in the scene, including their refractive indices. Exactly as optical pulses, synthetic pulses slow down when passing through materials with higher refractive indices. The experiments shown in Fig. 3i-l demonstrate this effect: Similar to Fig. 2, a diffuser is illuminated with a point source from behind, but now an additional $\sim 1mm$ thick glass slide covers a part of the diffuser. The respective SLiF video (see Fig. 3j and full video [here](#) [40]) shows that the synthetic pulse front travelling through both diffuser and glass slide is clearly delayed with respect to the pulse front that only travels through the diffuser, which is caused by the increased optical path length introduced by the glass. Figures 3k and l show the same effect, but demonstrate additional forms to decode the increased optical path length with synthetic pulse shaping. In Fig. 3k, the original spherical pulse front is computationally reshaped to a planar pulse front with a tilt in the vertical direction. When propagating through the flat diffuser with glass slide, the pulse front creates a horizontal “scan line” which experiences a vertical offset from the increased optical path length in the glass. In Fig. 3l the diffuser is illuminated with a bunny-shaped wavefront. While this experiment is meant to emphasize the flexibility of the approach (i.e., arbitrary spatial pulse shapes are possible), a clear pulse front offset from the glass slide is still visible in the bunny profile.

Although not shown here for the sake of brevity, *temporal* pulse shaping could also be exploited to further decode potentially important information in this scene. For example, a “double-peak” pulse front could be engineered where the temporal difference between both peaks exactly lines up with the optical path length difference introduced by the glass slide. For a pulse with a planar-shaped front parallel to the diffuser surface, this would mean that the glass slide and diffuser surface flash up at the exact same time stamp. This procedure could be used to detect thickness or refractive index variations in the glass slide. We believe that quantifying material properties with synthetic pulses has important potential application in the characterization of optical components (e.g., testing of multi-surface lens system, optical flats or mirrors), or the characterization of thin film materials [47]. Moreover, the “sectioning” ability of synthetic pulses paired with their robustness to scattering could potentially lead to impactful applications in medical imaging, such as novel pump-and-probe methods or virtual, optical stain-free histology which would not require slicing the sample and could potentially even be performed in-vivo.

4. CONCLUSION

We presented a novel approach that exploits multiple synthetic field measurements to generate “synthetic pulses”, used to ren-

der “Synthetic Light-in-Flight” (SLiF) videos of the synthetic pulse traveling through arbitrary scenes (including volumetric 3D scenes, scattering scenes, and scenes with varying refractive indices). Our demonstrated method does not rely on pulsed lasers or expensive high-speed detectors and requires only tunable CW lasers and ordinary CMOS detectors. Our SLiF measurements display infinite frame resolution (no camera frame rate restriction) and we have experimentally demonstrated sub- ps temporal resolution of up to $0.57ps$. This value is only dependent on the tuning range of the used lasers and can be easily improved with other hardware in future experiments. Besides showing basic synthetic pulse generation, we demonstrated how each individually captured synthetic field can be freely manipulated in the computer after its acquisition to shape the synthetic pulse in space and time, which can be used to efficiently decode specific information about the captured scene. We emphasize that all of our pulse measurements have been demonstrated in fairly small measurement volumes with a maximal size of $8 \times 8 \times 8cm^3$, which is another indicator for the remarkable temporal resolution capabilities of SLiF. These capabilities enable multiple potential applications in medical imaging, NLoS imaging, imaging through scattering media, material characterization, and automotive sensing. Similar to existing approaches in interferometric LiF imaging [1, 3, 4], our method bears resemblance to optical coherence tomography [48], coherence radar [49], and white light interferometry [50], however, with the important distinctions that our measurements are always performed full-field (no raster scanning or B-scan), and that each synthetic field is acquired individually which allows for the described free computational pulse manipulation in post-processing (temporal and spatial pulse shaping).

Of course, our method is not without limitations. A current bottleneck is the large number of synthetic fields that needs to be acquired for one single SLiF measurement, which currently restricts SLiF to strictly static scenes. Another restriction of technical origin is the power of our tunable lasers, which would need to be significantly increased to perform SLiF measurements in larger scenes such as rooms or traffic settings. Our future work will seek to address these limitations.

Due to the brevity of this letter we have limited ourselves to introducing the numerous new SLiF concepts and SLiF’s unique and diverse capabilities, but refrained from an extensive performance analysis which will be part of further publications tied to specific applications of SLiF. In the future, we hope that the capabilities introduced by SLiF can be further used to advance multiple fields in computational imaging and potentially spawn a new breed of computational cameras to image and quantify ultrafast processes.

REFERENCES

1. N. Abramson, “Light-in-flight recording by holography,” *Opt. Lett.* **3**, 121 (1978).
2. N. Abramson, “Light-in-flight recording: high-speed holographic motion pictures of ultrafast phenomena,” *Appl. Opt.* **22**, 215–232 (1983). Publisher: Optica Publishing Group.
3. G. Häusler, J. Herrmann, R. Kummer, and M. Lindner, “Observation of light propagation in volume scatterers with 10^{11} -fold slow motion,” *Opt. Lett.* **21**, 1087 (1996).
4. T. Inoue, T. Kakue, K. Nishio, *et al.*, “Recent Advances in Imaging of Light Propagation with Light-in-Flight Recording by Holography,” *Ultrafast Sci.* **3**, 0043 (2023). Publisher: American Association for the Advancement of Science.

5. D. Faccio and A. Velten, "A trillion frames per second: The techniques and applications of light-in-flight photography," *Reports on Prog. Phys.* **81**, 105901 (2018).
6. J. Liang, L. Zhu, and L. V. Wang, "Single-shot real-time femtosecond imaging of temporal focusing," *Light. Sci. & Appl.* **7**, 42 (2018).
7. G. Satat, B. Heshmat, D. Raviv, and R. Raskar, "All photons imaging through volumetric scattering," *Sci. reports* **6**, 33946 (2016).
8. A. Bocolini, F. Tonolini, J. Leach, *et al.*, "Imaging inside highly diffusive media with a space and time-resolving single-photon sensor," in *Imaging Systems and Applications*, (Optica Publishing Group, 2017), pp. ITu3E-2.
9. K. Wilson, B. Little, G. Gariepy, *et al.*, "Slow light in flight imaging," *Phys. Rev. A* **95**, 023830 (2017).
10. J. Liu, M. Marquez, Y. Lai, *et al.*, "Swept coded aperture real-time femtophotography," *Nat. Commun.* **15**, 1589 (2024).
11. A. Malik, N. Juravsky, R. Po, *et al.*, "Flying with Photons: Rendering Novel Views of Propagating Light," (2024). ArXiv:2404.06493 [cs, eess].
12. A. Velten, D. Wu, A. Jarabo, *et al.*, "Femto-photography: capturing and visualizing the propagation of light," *ACM Trans. Graph.* **32**, 44:1-44:8 (2013).
13. A. Pifferi, D. Contini, A. D. Mora, *et al.*, "New frontiers in time-domain diffuse optics, a review," *J. Biomed. Opt.* **21**, 091310 (2016). Publisher: SPIE.
14. G. Gariepy, N. Krstajić, R. Henderson, *et al.*, "Single-photon sensitive light-in-flight imaging," *Nat. communications* **6**, 6021 (2015).
15. B. Heshmat, G. Satat, C. Barsi, and R. Raskar, "Single-shot ultrafast imaging using parallax-free alignment with a tilted lenslet array," in *CLEO: Science and Innovations*, (Optica Publishing Group, 2014), pp. STu3E-7.
16. L. Gao, J. Liang, C. Li, and L. V. Wang, "Single-shot compressed ultrafast photography at one hundred billion frames per second," *Nature* **516**, 74-77 (2014).
17. M. O'Toole, D. B. Lindell, and G. Wetzstein, "Confocal non-line-of-sight imaging based on the light-cone transform," *Nature* **555**, 338-341 (2018). Publisher: Nature Publishing Group.
18. D. Faccio, A. Velten, and G. Wetzstein, "Non-line-of-sight imaging," *Nat. Rev. Phys.* **2**, 318-327 (2020).
19. D. B. Lindell, G. Wetzstein, and M. O'Toole, "Wave-based non-line-of-sight imaging using fast fk migration," *ACM Trans. on Graph. (ToG)* **38**, 1-13 (2019).
20. X. Liu, I. Guillén, M. La Manna, *et al.*, "Non-line-of-sight imaging using phasor-field virtual wave optics," *Nature* **572**, 620-623 (2019).
21. A. Velten, T. Willwacher, O. Gupta, *et al.*, "Recovering three-dimensional shape around a corner using ultrafast time-of-flight imaging," *Nat. Commun.* **3**, 745 (2012). Publisher: Nature Publishing Group.
22. D. B. Lindell and G. Wetzstein, "Three-dimensional imaging through scattering media based on confocal diffuse tomography," *Nat. communications* **11**, 4517 (2020).
23. E. Arons and D. Dilworth, "Analysis of fourier synthesis holography for imaging through scattering materials," *Appl. optics* **34**, 1841-1847 (1995).
24. M. P. Shih, H. S. Chen, and E. N. Leith, "Spectral holography for coherence-gated imaging," *Opt. letters* **24**, 52-54 (1999).
25. J. C. Marron and K. S. Schroeder, "Three-dimensional lensless imaging using laser frequency diversity," *Appl. optics* **31**, 255-262 (1992).
26. A. F. Fercher, H. Z. Hu, and U. Vry, "Rough surface interferometry with a two-wavelength heterodyne speckle interferometer," *Appl. optics* **24**, 2181-2188 (1985).
27. R. Dändliker, R. Thalmann, and D. Prongué, "Two-wavelength laser interferometry using superheterodyne detection," *Opt. letters* **13**, 339-341 (1988).
28. F. Willomitzer, P. V. Rangarajan, F. Li, *et al.*, "Fast non-line-of-sight imaging with high-resolution and wide field of view using synthetic wavelength holography," *Nat. Commun.* **12**, 6647 (2021).
29. F. Willomitzer, F. Li, M. M. Balaji, *et al.*, "High resolution non-line-of-sight imaging with superheterodyne remote digital holography," in *Computational Optical Sensing and Imaging*, (Optica Publishing Group, 2019), pp. CM2A-2.
30. F. Willomitzer, "Synthetic wavelength imaging: Utilizing spectral correlations for high-precision time-of-flight sensing," *Comput. Imaging for Scene Understanding: Transient, Spectral, Polarim. Anal.* p. 187 (2024).
31. M. Ballester, H. Wang, J. Li, *et al.*, "Single-shot synthetic wavelength imaging: Sub-mm precision tof sensing with conventional cmos sensors," *Opt. Lasers Eng.* **178**, 108165 (2024).
32. P. Rangarajan, F. Willomitzer, O. Cossairt, and M. P. Christensen, "Spatially resolved indirect imaging of objects beyond the line of sight," in *Unconventional and Indirect Imaging, Image Reconstruction, and Wavefront Sensing 2019*, vol. 11135 (SPIE, 2019), pp. 124-131.
33. F. Li, F. Willomitzer, M. M. Balaji, *et al.*, "Exploiting wavelength diversity for high resolution time-of-flight 3d imaging," *IEEE Trans. on Pattern Anal. Mach. Intell.* **43**, 2193-2205 (2021).
34. F. Li, F. Willomitzer, P. Rangarajan, *et al.*, "Sh-tof: Micro resolution time-of-flight imaging with superheterodyne interferometry," in *2018 IEEE International Conference on Computational Photography (ICCP)*, (IEEE, 2018), pp. 1-10.
35. A. Kotwal, A. Levin, and I. Gkioulekas, "Swept-angle synthetic wavelength interferometry," in *Proceedings of the IEEE/CVF Conference on Computer Vision and Pattern Recognition*, (2023), pp. 8233-8243.
36. A. Gröger, G. Pedrini, F. Fischer, *et al.*, "Two-wavelength digital holography through fog," *J. Eur. Opt. Soc. Publ.* **19**, 25 (2023).
37. P. De Groot and J. McGarvey, "Chirped synthetic-wavelength interferometry," *Opt. letters* **17**, 1626-1628 (1992).
38. P. Cornwall, M. Ballester, H. Wang, and F. Willomitzer, "Towards synthetic light-in-flight," in *Computational Optical Sensing and Imaging*, (Optica Publishing Group, 2023), pp. CTh2B-3.
39. S. Forschner, P. Cornwall, M. M. Balaji, *et al.*, "Towards synthetic wavelength imaging through multi-mode fibers," *Proceedings of the 14th International Conference on Optics-photonics Design and Fabrication (ODF)* (2024).
40. "Video repository for this paper," Video (2024). <https://drive.google.com/drive/folders/1Nm6MK2ZsYlDEgLyq00DVy0KtVHMU4dxr?usp=sharing>.
41. J. N. Mait, G. W. Euliss, and R. A. Athale, "Computational imaging," *Adv. Opt. Photonics* **10**, 409-483 (2018).
42. C. Wagner and G. Häusler, "Information theoretical optimization for optical range sensors," *Appl. optics* **42**, 5418-5426 (2003).
43. G. Häusler and F. Willomitzer, "Reflections about the holographic and non-holographic acquisition of surface topography: where are the limits?" *Light. Adv. Manuf.* **3**, 226-235 (2022).
44. K. B. Hill and D. J. Brady, "Pulse shaping in volume reflection holograms," *Opt. letters* **18**, 1739-1741 (1993).
45. K. B. Hill, K. G. Purchase, and D. J. Brady, "Pulsed-image generation and detection," *Opt. letters* **20**, 1201-1203 (1995).
46. M. Gupta, A. Velten, S. K. Nayar, and E. Breitbart, "What are optimal coding functions for time-of-flight imaging?" *ACM Trans. on Graph. (TOG)* **37**, 1-18 (2018).
47. J. M. Bass, M. Ballester, S. M. Fernández, *et al.*, "An angular spectrum approach to inverse synthesis for the characterization of optical and geometrical properties of semiconductor thin films," arXiv preprint arXiv:2407.06535 (2024).
48. D. Huang, E. A. Swanson, C. P. Lin, *et al.*, "Optical coherence tomography," *science* **254**, 1178-1181 (1991).
49. T. Dresel, G. Häusler, and H. Venzke, "Three-dimensional sensing of rough surfaces by coherence radar," *Appl. optics* **31**, 919-925 (1992).
50. L. Deck and P. De Groot, "High-speed noncontact profiler based on scanning white-light interferometry," *Appl. optics* **33**, 7334-7338 (1994).